(Preprint) AAS 21-677

CHARACTERIZATION OF BALLISTIC CAPTURE CORRIDORS AIMING AT AUTONOMOUS BALLISTIC CAPTURE AT MARS

Gianmario Merisio[*] and Francesco Topputo[†]

Current deep-space missions heavily count on ground-based operations. Although reliable, ground slots will saturate soon, so hampering the current momentum in space exploration. EXTREMA, a project awarded an ERC Consolidator Grant in 2019, enables self-driving spacecraft, challenging the current paradigm and aiming, among others, at autonomously engineering ballistic capture. This work presents the characterization of ballistic capture corridors, time-varying manifolds that support capture. A preliminary methodology to approximate such entities is proposed. Results show that a mapping between corridor states and capture set initial conditions is attainable. This is a first effort in the development of an on-board autonomous ballistic capture algorithm suitable for spacecraft with limited control authority and on-board resources like CubeSats.

INTRODUCTION

The space sector is experiencing flourishing growth and evidence is mounting that the near future will be characterized by a large amount of deep-space missions.[1–3] In the last decade, CubeSats have granted affordable access to space due to their reduced manufacturing costs compared to traditional missions. At the present-day, most miniaturized spacecraft has thus far been deployed into near-Earth orbits, but soon a multitude of interplanetary CubeSats will be employed for deep-space missions as well. However, the current paradigm for deep-space missions strongly relies on ground-based operations. Although reliable, this approach will rapidly cause saturation of ground slots, hampering the current momentum in space exploration.

EXTREMA (short for *Engineering Extremely Rare Events in Astrodynamics for Deep-Space Missions in Autonomy*) enables self-driving spacecraft, challenging the current paradigm under which spacecraft are piloted in the interplanetary space. Deep-space guidance, navigation, and control (GNC) applied in a complex scenario is the subject of EXTREMA, which wants to engineer ballistic capture (BC) in a totally autonomous fashion. EXTREMA is erected on three pillars. Pillar 1 is on autonomous navigation. Pillar 2 involves autonomous guidance and control. Pillar 3 deals with autonomous BC, the focus of this work. The project has been awarded a European Research Council (ERC) Consolidator Grant in 2019.

BC allows a spacecraft to approach a planet and enter a temporary orbit about it without requiring maneuvers in between. As part of the low-energy transfers, it is a valuable alternative to Keplerian approaches. Exploiting BC grants several benefits in terms of both cost reduction[4] and mission versatility,[5,6] in general at the cost of longer transfer times.[7,8] In the past, BC mechanism was used to rescue Hiten,[9] and to design insertion trajectories in lunar missions like SMART-1[10] and GRAIL.[11] More recently, BC orbits were proposed for BepiColombo,[12] Lunette,[13] and ESMO[14] missions. BC is closely connected to the weak stability boundary (WSB) concept.[15] To date, despite the effort spent in the past years, both WSB and BC are still not completely understood.

BC mechanism is suited for limited-control platforms, which cannot afford to enter into orbits about a planet because of the lack of proper means. BC is an event that occurs in extremely rare occasions and

[*]PhD Student, Department of Aerospace Science and Technology, Politecnico di Milano, Via La Masa 34, 20156, Milan, Italy, gianmario.merisio@polimi.it.
[†]Full Professor, Department of Aerospace Science and Technology, Politecnico di Milano, Via La Masa 34, 20156, Milan, Italy, francesco.topputo@polimi.it.

requires acquiring a proper state (position and velocity) far away from the target planet.[6] Massive numerical simulations are required to find the specific conditions that support capture.[16] On average, 1 out of 10000 conditions explored by the algorithm grants capture.[17]

The union of those points defines the capture set, which in turn is used to find a ballistic capture corridor (BCC). BCCs (sometimes referred to as corridors) are streams of trajectories that can be targeted far away from the planet and that guarantee BC. From a different perspective, BCCs are time-varying manifolds that support capture. These manifolds are rare, narrow, flat hyper-tubes located in the phase space, which are obtained propagating backward initial conditions (ICs) belonging to capture sets. The present method is definitely not keen for on-board applications.

This paper is focused on the Pillar 3 of EXTREMA. In Pillar 3, it is investigated how spacecraft can attain BC in autonomy. The spacecraft assumed already in deep space has to acquire BC at Mars without relying on any information provided from the ground. Mars is chosen without loss of generality due to its relevance in long-term exploration. The method based on stable sets is preferred due to its versatility: it works for any model, energy, and epoch.[17] The challenge is to develop and validate an algorithm compatible with on-board resources. In this work, BCCs at Mars are characterized as a first step in the development of such algorithm.

Capture sets at Mars were found via grid sampling and propagation in the solar system restricted n-body problem accounting for solar radiation pressure (SRP) and Mars' non-spherical gravity (NSG) perturbations following the methodology presented in Reference 18. Favorable Mars's true anomaly, orbital plane, and eccentricity were exploited to enhance the *quantity* (number) and *quality* (regularity) of the specific conditions granting capture.[17] Corridors were computed via backward propagation, still in the high-fidelity model. The streams of backward propagated trajectories was then characterized and numerically approximated. Far from capture, the resulting parametric surfaces were proven to be smooth and well suited for mapping corridor states to capture set ICs.

DYNAMICAL MODEL

Following the nomenclature in Reference 18, a *target* and a *primary* were defined. The target is the body around which the ballistic capture is studied. The primary is the main body around which the target revolves. Target and primary masses are m_t and m_p respectively. The mass ratio of the system is $\mu = m_t/(m_t + m_p)$. This work is focused on ballistic capture having Mars as target and the Sun as primary*.

Reference frames

The following reference frames were used: J2000, ECLIPJ2000, RTN@t_i, and RPF.

J2000. Defined on the Earth's mean equator and equinox, the J2000 is an inertial frame determined from observations of planetary motions which was realized to coincide almost exactly with the International Celestial Reference Frame (ICRF).[19] The J2000 inertial frame (also known as EMEJ2000) is built-in in SPICE†.[20,21] In SPICE, the ICRF and J2000 frames are considered the same. The center of the J2000 can be chosen arbitrarily. The equations of motion are integrated in this reference frame.

ECLIPJ2000. This is an inertial frame built-in in SPICE which is defined on the ecliptic coordinates and based on the J2000 inertial frame. The origin of the ECLIPJ2000 frame can be chosen arbitrarily.

RTN@t_i. The radial-tangential-normal of date frame (RTN@t_i) is an inertial frame frozen at a prescribed epoch t_i. The frame is centered at the target. The x-axis is aligned with the primary–secondary direction, the z-axis is normal to the primary–secondary plane in the direction of their angular momentum, and the y-axis completes the dextral orthonormal triad. ICs are defined in this frame.[17] The RTN@t_i frame was defined in SPICE such that transformation matrices between this and other frames could be easily obtained trough dedicated SPICE's routines.

*See Table 2 in Reference 18 for a complete list of targets and their primaries.

†SPICE is the information system developed by Navigation and Ancillary Information Facility (NAIF) to assist NASA scientists and engineers in mission modeling, planning, interpreting scientific observations, and executing activities. `https://naif.jpl.nasa.gov/naif/` [last accessed 30/07/2021]

Table 1. Assumed spacecraft specifications.

Specification	Symbol	Value
Mass	m	24 kg
SRP area	A	0.32 m^2
Coefficient of reflectivity	C_r	1.3

RPF. The roto-pulsating frame (RPF) is a rotating frame centered at the primary–target system barycenter. The rotation is such that both the target and the primary are at rest in the RPF. In this frame, the x-axis points from the primary to the target, the z-axis is directed as the angular momentum of the system, and the y-axis completes the dextral orthonormal triad. The transformation from and to the RPF is not trivial. Indeed, it involves a change of origin, a rotation, and a scaling.[22]

Ephemerides

For this work the precise states of the Sun and the major planets were retrieved from the Jet Propulsion Laboratory (JPL)'s planetary ephemerides `de440s.bsp`* (or DE440s).[23] Additionally, the ephemerides `mars097.bsp` of Mars (the target) and its moons were employed†. The following generic leap seconds kernel (LSK) and planetary constants kernel (PCK) were used: `naif0012.tls`, `pck00010.tpc`, and `gm_de431.tpc`‡.

Equations of motion

The equations of motion used are those of the restricted n-body problem. The gravitational attractions of the Sun, Mercury, Venus, Earth (B§), Mars (central body), Phobos, Deimos, Jupiter (B), Saturn (B), Uranus (B), Neptune (B) were considered. Additionally, SRP and Mars' NSG were also included in the model. The assumed spacecraft specifications needed to evaluate the SRP perturbation are collected in Table 1. They are compatible with the specifications of a 12U deep-space CubeSat.[24] The terms of the infinite series modeling NSG were considered up to degree $n_{\text{deg}} = 20$ and order $n_{\text{ord}} = 20$. The coefficients to evaluate the NSG perturbation were retrieved from the MRO120D gravity field model of Mars. Data are publicly available in the file `jgmro_120d_sha.tab`, archived in the Geosciences Node of National Aeronautics and Space Administration (NASA)'s Planetary Data System (PDS)¶. Far from Mars, when not in a temporary capture condition, gravitational attractions of Phobos and Deimos, and Mars' NSG perturbation were neglected.

The equations of motion, written in a non-rotating Mars-centered reference frame are[18,25]

$$\ddot{\mathbf{r}} = -\frac{\mu_t}{r^3} - \sum_{i\in\mathbb{P}} \mu_i \left(\frac{\mathbf{r}_i}{r_i^3} + \frac{\mathbf{r}-\mathbf{r}_i}{\|\mathbf{r}-\mathbf{r}_i\|^3} \right) + \frac{QA}{m} \frac{\mathbf{r}-\mathbf{r}_\odot}{\|\mathbf{r}-\mathbf{r}_\odot\|^3} - \mathcal{R}\frac{\mu_t}{r^2} \left(\Lambda \frac{\mathbf{r}}{r} - \begin{bmatrix} J \\ K \\ H \end{bmatrix} \right) \tag{1}$$

where μ_t is the gravitational parameter of the target body (Mars in this work); $\mathbf{r}$ is the position vector of the spacecraft with respect to the target and r is its magnitude; $\mathbb{P}$ is a set of $n-2$ indexes each referring to a perturbing body; μ_i and $\mathbf{r}_i$ are the gravitational parameter and position vector with respect to the target of the i-th body, respectively; A is the Sun-projected area on the spacecraft for SRP evaluation; m is the spacecraft mass; $\mathbf{r}_\odot$ is the position vector of the Sun with respect to the target; $\mathcal{R}$ is the time-dependent

*Data publicly available at: `https://naif.jpl.nasa.gov/pub/naif/generic_kernels/spk/planets/de440s.bsp` [retrieved 30/07/2021].

†`~/spk/satellites/mars097.bsp` [retrieved 30/07/2021].

‡Data publicly available at: `https://naif.jpl.nasa.gov/pub/naif/generic_kernels/lsk/naif0012.tls`, `~/generic_kernels/pck/pck00010.tpc`, and `~/generic_kernels/pck/gm_de431.tpc` [retrieved 30/07/2021]. The `gm_de431.tpc` PCK kernel was used because the new version consistent with the ephemerides DE440s was not released yet.

§Here B stands for barycenter.

¶Data publicly available at: `https://pds-geosciences.wustl.edu/mro/mro-m-rss-5-sdp-v1/mrors_1xxx/data/shadr/` [retrieved 30/07/2021].

Table 2. Normalization units.

Unit	Symbol	Value	Comment
Gravity parameter	MU	$42\,828.376\,\mathrm{km^3\,s^{-2}}$	Mars' gravity parameter
Length	LU	3396.0000 km	Mars' radius
Time	TU	956.281 42 s	$(\mathrm{LU}^3/\mathrm{MU})^{0.5}$
Velocity	VU	$3.551\,255\,8\,\mathrm{km\,s^{-1}}$	LU/MU

matrix transforming vector components from the Mars-fixed frame to the non-rotating frame in which the equations of motion are written; Λ, J, K, and H are defined as in Reference 26. Lastly, Q is equal to

$$Q = \frac{LC_r}{4\pi c} \tag{2}$$

where C_r is the spacecraft coefficient of reflectivity, $c = 299\,792\,458\,\mathrm{m\,s^{-1}}$ (from SPICE[20,21]) is the speed of light in vacuum, and $L = S_\odot 4\pi d_{\mathrm{AU}}^2$ is the luminosity of the Sun. The latter is computed from the solar constant* $S_\odot = 1367.5\,\mathrm{W\,m^{-2}}$ evaluated at $d_{\mathrm{AU}} = 1\,\mathrm{AU} = 149\,597\,870\,613.6889\,\mathrm{m}$ (from SPICE[20,21]).

Numerical integration of the equations of motion

The equations of motion in Eq. (1) were integrated with GRavity TIdal Slide (GRATIS) tool[27] in their nondimensional form to avoid ill-conditioning.[18] The normalization units specifically used for this work are reported in Table 2. Numerical integration was carried out either with MATLAB®'s `ode113`[28] or with `ode78` routine implementing the Dormand-Prince 8th-order embedded Runge-Kutta method propagation scheme,[29] also known as RK8(7)13M†. The former is a multistep, variable-step variable-order, Adams-Bashforth-Moulton, predictor-corrector solver of orders 1st to 13th‡. The latter is an adaptive step, 8th-order RK integrator with 7th-order error control. The coefficients were derived by Prince and Dormand.[30] MATLAB®'s `ode113` was used to derive the capture sets and in the preliminary investigation of corridors, while `ode78` was used in the characterization of the corridors and in their numerical approximation. The dynamics were propagated with relative and absolute tolerances both set to 10^{-12}.[18]

CHARACTERIZATION OF BALLISTIC CAPTURE CORRIDORS

A BCC is a moving manifolds that supports capture. A corridor is obtained backward propagating ICs belonging to a capture sets $\mathcal{C}_{-1}^n$, where $n > 0$ is the number of revolutions after being captured. A capture set is defined as $\mathcal{C}_{-1}^n = \mathcal{W}^n \cap \mathcal{X}_{-1}$. Therefore, it is the intersection between the stable set in forward time $\mathcal{W}_n$ and the unstable set in backward time $\mathcal{X}_{-1}$.[18] They are defined accordingly to the algorithmic definition of WSB.[16] Similarly to how capture sets are symbolically designated, a corridor developed from a capture set $\mathcal{C}_{-1}^n$ is indicated as $\check{\mathcal{B}}_{-1}^n$.

In this work, two corridors were built and characterized starting from two peculiar capture sets. The capture sets were constructed from the same initial grid following the methodology discussed in Reference 18. The grid of ICs was chosen to maximize the capture ratio $\mathcal{R}_c$ based on the analysis reported in Reference 17. The capture epoch was chosen to be the JD 2460287.53156250 (UTC), corresponding to the 09 DEC 2023 00:45:18.363 (UTC). At that epoch, Mars's true anomaly with respect to the Sun is equal to 270 deg, maximizing $\mathcal{R}_c$.[17] In a similar fashion, the inclination i_0 and the right ascension of the ascending node (RAAN) Ω_0 of the orbital plane of the initial osculating orbits were taken both equal to 0.2π rad. That because, according

*`https://extapps.ksc.nasa.gov/Reliability/Documents/Preferred_Practices/2301.pdf` [last accessed 30/07/2021].

†The notation RK$p(q)s$M is used when referring to a Runge-Kutta method of order p, with an embedded step-size control of qth-order, and a total of s stages.[29]

‡The highest order used appears to be 12th since a formula of order 13th is used to form the error estimate and the function does local extrapolation to advance the integration at order 13th. `https://it.mathworks.com/help/matlab/ref/ode113.html` [last accessed 30/07/2021].

to Figure 10 in Reference,[17] such values maximize the capture ratio for Mars. The initial osculating eccentricity e_0 was fixed equal to 0.99.[6] Finally, a discretization of pericenter r_0 and argument of pericenter ω_0 was assumed to build the initial grid. r_0 was discretized in the interval $[R_t + \varepsilon, 10R_t]$ with step $\Delta r_0 = 100\,\text{km}$ ($\varepsilon = 100\,\text{km}$). ω_0 was discretized in the interval $[0, 2\pi)$ with step $\Delta\omega = 1\,\text{deg}$ (or $\approx 0.0175\,\text{rad}$). The grid was made of $N_{r_0} = 339$ and $N_{\omega_0} = 360$ evenly spaced points of r_0 and ω_0, respectively. Each IC was assumed to be the pericenter of an osculating orbit, and therefore having true anomaly $\theta_0 = 0$.

The characterization process consisted of the following: *i*) critical analysis of trends and rates of corridor's osculating elements when orbiting the Sun; *ii*) visualization of *time snapshots* of corridor's heliocentric Keplerian elements and consequent pattern identification; *iii*) opportunistic selection of a circular domain in the capture sets to derive the corresponding *subcorridor* (subset of a corridor); *iv*) investigation of subcorridor's dimensions and determination of its shape; *v*) visualization of subcorridor's Poincaré sections and related critical analysis; *vi*) parametric representation and numerical approximation of a subcorridor.

Step *i*) trends and rates of Keplerian elements

The first step of the characterization provided a first look into the behavior of the corridor when observed in heliocentric coordinates. The expectation was to observe trajectories similar to each other far from the target body. That because a spacecraft is affected mainly by the Sun's gravitational attraction when far from Mars. Consequently, the features of highly chaotic trajectories, essential elements of the BC phenomenon, should not be observed far from the target body. Additionally, the rates of the Keplerian elements were computed using a finite differences scheme to further confirm how variations of corridor's Keplerian elements are small far from the central body.

Step *ii*) time snapshots

The dynamics being non-autonomous, a *time snapshot* is a collection of states taken at a fixed time epoch. Based on the considerations made for the previous step of the characterization, the time snapshots of a corridor's heliocentric Keplerian elements were expected to show some patterns. Specifically, the aim of this step was to visualize how states spread in a time snapshots, assessing by visual inspection if the clusters of ICs rifted apart or stayed connected. Due to the presence of many clusters of ICs typical of capture sets and the potential Cantor-like structure claimed in Reference 31, a corridor was expected to be made of various subsets. However, the major concern was to find *holes* in their structure, recognizing such subsets as not continuous entities.

Step *iii*) opportunistic selection of a corridor subset

A subcorridor $\check{\mathcal{S}}^n_{-1}$, subset of a corridor $\check{\mathcal{B}}^n_{-1}$, was investigated in more details. A circular domain within the capture set was opportunistically chosen to derive the corresponding subcorridor. Location and size of the domain were selected based on the local value of regularity index* S and regularity coefficient $\Delta S_{\%}$ of the capture set. Regularity index and coefficient are defined as[33]

$$S = \frac{t_{N_r} - t_0}{N_r}, \qquad S^{(2b)} = \frac{2\pi}{\sqrt{\mu_t}} \left(\frac{r_0}{1 - e_0} \right)^{3/2}, \qquad \Delta S_{\%} = 100 \left| \frac{S}{S^{(2b)}} - 1 \right| \tag{3}$$

where N_r is the number of forward or backward revolutions, t_0 is the initial time, and t_{N_r} is the time required to complete the N_r revolutions. $S^{(2b)}$ is used as reference and correspond to the regularity index of a Keplerian orbit.[33] The smaller the regularity index and coefficient, the more regular the post-capture trajectory.

Step *v*) dimensions and shape of the subcorridor

Dimensions and shape of the subcorridor (for the sake of conciseness also referred to as corridor from now on) were investigated too. That to see how much its size increases or decreases with time, how much

*In literature, the regularity index is more commonly known as stability index.[17,18,32] However, in Reference 33, the adjustment from *stability* to *regularity* index was proposed to avoid misunderstandings with the periodic orbit stability index. The same nomenclature introduced in Reference 33 is used in this work.

the corridor is stretched, compressed, tilted, *etc*., what shape it takes on, and how the shape changes over time. Specifically, two- and three-dimensional representations of the corridor were plotted to get confidence with shape and sizes of corridors. The result was achieved visualizing the envelope $\partial\check{\mathcal{S}}^n_{-1}$ of the subcorridor. Envelope constructed sampling uniformly the subcorridor domain border with enough points, backward propagating them up to a desired final time before capture, and collecting all the propagated trajectories.

Step *iv*) subcorridor's Poincaré sections

Poincaré sections of the subcorridor were computed at prescribed solar longitudes λ. The selection of longitude values was performed based on the physical space spanned by the corridor in the time frame of the backward propagation performed. Therefore, the corridor was intersected in the physical space by half-planes originating from the z-axis. The shapes of these *cuts* in the physical space were derived and plotted for various solar longitudes. Velocity surfaces corresponding to Poincaré sections were computed too. Differently from time snapshots, corridor's trajectories reach the Poincaré sections at different time epochs. Poincaré sections were computed because they were expected to provide precise estimates of corridor dimensions and a clear insight on its shape.

Step *vi*) subcorridor parametric representation and numerical approximation

A numerical approximation of the corridor was built with the aim of a future on-board implementation of a BCCs database. Firstly, a parametric representation of the corridor was carried out. Then, an interpolation between two corridor's Poincaré sections was performed to derive an intermediate section. Finally, states on the interpolated sections were retrieved via a second interpolation.

The corridor was represented through parametric surfaces, miming what was done in Reference 34 but applying the methodology to a non-autonomous system instead of an autonomous one. The Cartesian coordinates x_0 and y_0 were used as parameters*. They are two independent variables that describe the locations of ICs on the orbital plane in which the capture set is defined. Given a Poincaré sections and the corresponding solar longitude λ, that corridor's section is completely described by six variables, namely the time interval from t_0 (or alternatively the time epoch), the projection of the position vector on the xy-plane (computed as $\sqrt{x^2+y^2}$), the third component of the position vector z, and the three velocity components v_x, v_y, and v_z. In this way, the corridor's state on a Poincaré section were suitably mapped to the corresponding states at capture.

The grid used to numerically represent the parametric surfaces were constructed sampling the subcorridor domain with a Fibonacci lattice and subsequently performing a Delaunay triangulation. The Fibonacci lattice is a mathematical idealization of the *sunflower* pattern. It can be generated with the following formulae[35]

$$l_i = l_0\sqrt{i-1/2} \tag{4}$$

$$\phi_i = 2\pi i\Phi^{-1} \tag{5}$$

where l_i and ϕ_i are the radial and azimuthal polar coordinate of each point i of the grid, while $\Phi = 1+\Phi^{-1}$ is the golden ratio equal to $(1+\sqrt{5})/2$. The Fibonacci grid was chosen for its several attributes, namely its geometric regularity, the almost homogeneous and isotropic resolution, and a lack of artificial symmetries. All features that make the lattice suitable for numerical modeling.[35]

Given two Poincaré sections 1 and 2 separated by an angle $\Delta\lambda = \lambda_2 - \lambda_1$ small, thereby enough close too each other, the intermediate section at $\lambda_i = (\lambda_1+\lambda_2)/2$ was derived by linear interpolation. The linear interpolation was carried out point by point between corresponding samples of the Fibonacci lattice. States on interpolated sections were evaluated by linearly interpolating the parametric surfaces numerically constructed on the Fibonacci lattice.

Finally, a test point was evaluated on the numerical approximation of the corridor to preliminary verify the goodness of numerical approximation itself. The test point was arbitrary chosen to be the center of the

*This is not the only available option. Also other couples of parameters could be used, *e. g.,* the pericenter r_{p0} and the argument of pericenter ω_0.

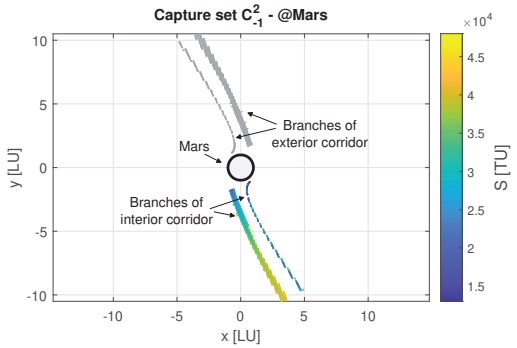

(a) Regularity index of ICs belonging to the two branches developing the interior ballistic capture corridor.

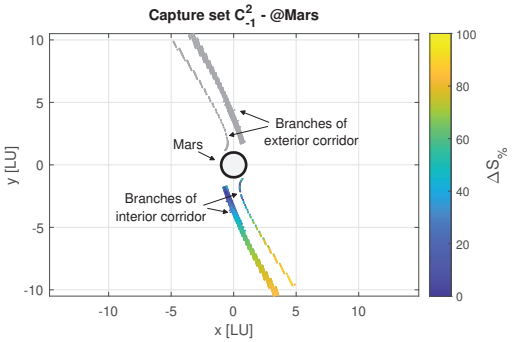

(b) Regularity coefficient of ICs belonging to the two branches developing the interior ballistic capture corridor.

Figure 1. Capture set $\mathcal{C}^2_{-1}$. Branches developing exterior ballistic capture corridors are colored in gray. ICs are represented in nondimensional quantities in the Mars-centered RTN@t_0 frame. Mars is the gray circle with black surround.

corridor since it is never a point of the Fibonacci lattice. The evaluations were compared against the high-fidelity solution propagated with GRATIS. The evaluation errors, called errors at insertion, were computed for any tested solar longitudes as

$$e_{t_i} = |t_i - t_i^*|, \quad e_{r_i} = \|\mathbf{r}_i - \mathbf{r}_i^*\|, \quad e_{v_i} = \|\mathbf{v}_i - \mathbf{v}_i^*\| \tag{6}$$

where t_i^*, $\mathbf{r}_i^*$, and $\mathbf{v}_i^*$ are the time epoch, position, and velocity of the high-fidelity solution, respectively. Additionally, also errors on time epoch and osculating elements at capture were estimated. They were computed between the new capture point*, obtained by forward propagating the evaluated test point, and the initial osculating elements of the test point at time epoch t_0. Hence

$$e_{t_0} = |t_0 - t_0^*|, \; e_{r_0} = |r_0 - r_0^*|, \; e_{e_0} = |e_0 - e_0^*|, \; e_{i_0} = |i_0 - i_0^*|, \; e_{\Omega_0} = |\Omega_0 - \Omega_0^*|, \; e_{\omega_0} = |\omega_0 - \omega_0^*| \tag{7}$$

where quantities marked with $*$ superscript are the exact initial time epoch and osculating elements.

RESULTS

The peculiar capture sets $\mathcal{C}^2_{-1}$ and $\mathcal{C}^6_{-1}$ from which corridors $\check{\mathcal{B}}^2_{-1}$ and $\check{\mathcal{B}}^6_{-1}$ were developed are shown in Figures 1 and 2, respectively. In the capture set $\mathcal{C}^2_{-1}$, four sickle-shaped clusters of ICs are distinguishable. The two of them located in the half-plane $y > 0$, colored in gray, develop the exterior corridor. Differently, the other two branches develop the interior corridor. On the other hand, set $\mathcal{C}^6_{-1}$ is made by only two clusters. The branch in the bottom half-plane gives rise to the interior corridor, while the gray one generates the exterior corridor.

An exterior corridor $\check{\mathcal{E}}^n_{-1}$ was defined as the subset of a corridor $\check{\mathcal{B}}^n_{-1}$ including heliocentric trajectories having semi-major axis a greater than Mars' one (equal to 1.5237 AU) after escaping from Mars in backward time. Contrarily, an interior corridor $\check{\mathcal{I}}^n_{-1}$ was defined as the subset of a corridor $\check{\mathcal{B}}^n_{-1}$ including all trajectories having semi-major axis smaller than Mars' one. Consequently, $\check{\mathcal{B}}^n_{-1} = \check{\mathcal{E}}^n_{-1} \cup \check{\mathcal{I}}^n_{-1}$. In the context of the EXTREMA project, interior corridors are more interesting because they extend between Mars and Earth's orbits.

In Figure 3, corridors $\check{\mathcal{B}}^2_{-1}$ and $\check{\mathcal{B}}^6_{-1}$ are shown. Interior and exterior corridors are colored in blue and yellow, respectively. As expected, $\check{\mathcal{B}}^2_{-1}$ looks thicker and more packed than $\check{\mathcal{B}}^6_{-1}$. That because of how stable

*To find the new capture point is not trivial. In fact, for a generic state, neither the capture epoch nor the capture point location are known a priori. Generally speaking, capture is not even granted. However, if the IC forward propagated still belongs to a corridor (any corridor), a new capture point can be found inverting the methodology to construct ballistic capture orbits.[18] Details are absent because out of the scope of this work.

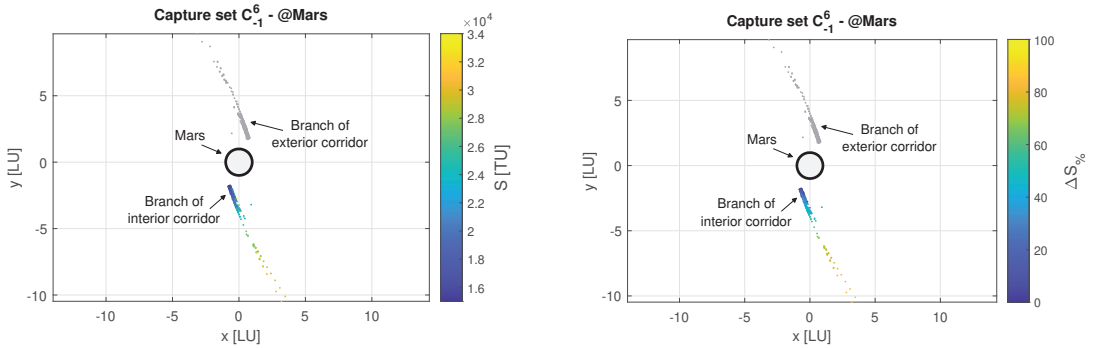

(a) Regularity index of ICs belonging to the branch developing the interior ballistic capture corridor.

(b) Regularity coefficient of ICs belonging to the branch developing the interior ballistic capture corridor.

Figure 2. Capture set $\mathcal{C}^6_{-1}$. Branches developing exterior ballistic capture corridors are colored in gray. ICs are represented in nondimensional quantities in the Mars-centered RTN@t_0 frame. Mars is the gray circle with black surround.

sets are defined.[36] Indeed, by definition of capture set, $\mathcal{C}^n_{-1} \subseteq \mathcal{C}^m_{-1}$ with m and n both positive, and $n > m$. Consequently, $\check{\mathcal{B}}^n_{-1} \subseteq \check{\mathcal{B}}^m_{-1}$ is verified too, therefore $\check{\mathcal{B}}^6_{-1}$ is a subset of $\check{\mathcal{B}}^2_{-1}$. In general, the same applies to $\check{\mathcal{I}}^n_{-1}$ and $\check{\mathcal{E}}^n_{-1}$.

Step *i*) trends and rates of Keplerian elements

Osculating elements of corridors about the Sun in the ECLIPJ2000 frame were computed to check their variation in time. Figure 4 shows the histories of the six Keplerian elements from t_0 to $t_0-1000\,\mathrm{d}$ of both $\check{\mathcal{B}}^2_{-1}$ and $\check{\mathcal{B}}^6_{-1}$. In the plots, histories are compared to Mars' orbit Keplerian elements. Except for initial short transients close to the capture epoch t_0 characterized by huge variations, all elements but true anomaly θ stabilize rapidly. After approximately 300 days in backward time, curves look completely flat. Such time span is in line with the typical time of flight on pre-capture legs belonging to the unstable set $\mathcal{X}_{-1}$. After the strong, short transient, true anomaly varies accordingly with Mar's true anomaly as expected. From the plots in the top-left corner of both Figure 4(a) and Figure 4(b), showing the trend of semi-major axis a, the distinction between interior and exterior corridors is clear. However, the four peculiar branches of $\mathcal{C}^2_{-1}$ cannot be distinguished within the two bundles of curves.

Previous statements are confirmed by the results in Figure 5 showing the yearly rates of the heliocentric osculating elements but the true anomaly. In the plots, they are compared to the yearly rates of Mars' orbit which are represented by the dotted horizontal lines. As expected, the strong, short transients are characterized by large rates as can be seen on the left hand side of Figures 5(a) and 5(b).

Step *ii*) time snapshots

Two time snapshots at $t = t_0-600\,\mathrm{d}$ were taken. One about $\check{\mathcal{B}}^2_{-1}$, found in Figure 6, and the other of $\check{\mathcal{B}}^6_{-1}$, visible in Figure 7. They show the instantaneous values of the Keplerian elements about the Sun in the ECLIPJ2000 frame of the two corridors 600 days before capture epoch at Mars. They correspond to the states at the end points of the trajectories in Figure 3.

Differently from what shown by Figure 4(a), in Figure 6 the four branches are easily identifiable. Interior and exterior corridors features are nearly symmetric. Indeed, they almost exhibit a point symmetry with respect to Mar's Keplerian elements, marked by red crosses. In this time snapshot, each branch is well resolved, thin, and relatively long. That is a peculiarity of this specific corridor and not a common feature. Indeed, numerical experiments here omitted showed that such characteristics are typical of highly regular capture sets like the ones used in this work (see Figure 1 and Figure 2). Differently, less regular capture sets

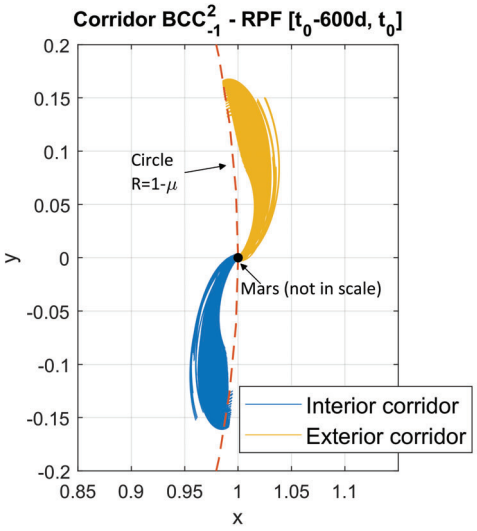

(a) Corridor $\check{\mathcal{B}}^2_{-1}$ developed by capture set $\mathcal{C}^2_{-1}$.

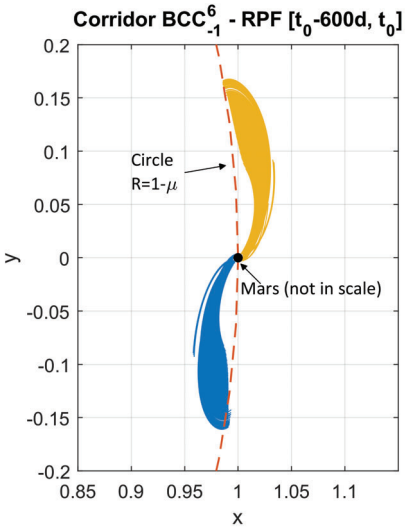

(b) Corridor $\check{\mathcal{B}}^6_{-1}$ developed by capture set $\mathcal{C}^6_{-1}$.

Figure 3. BCCs from t_0 to $t_0-600\,\mathrm{d}$. Interior and exterior corridors are colored in blue and yellow, respectively. Trajectories are represented in nondimensional coordinates in the RPF.

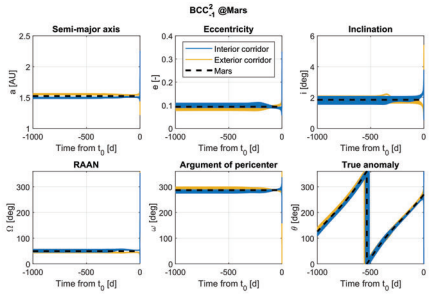

(a) Trends of heliocentric osculating elements of $\check{\mathcal{B}}^2_{-1}$.

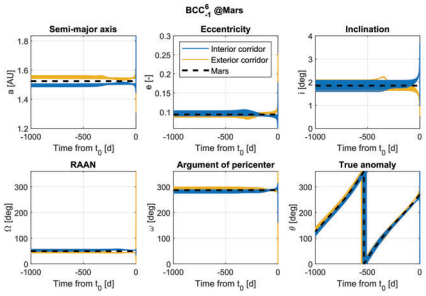

(b) Trends of heliocentric osculating elements history of $\check{\mathcal{B}}^6_{-1}$.

Figure 4. Trends of heliocentric osculating elements of BCCs from t_0 to $t_0-1000\,\mathrm{d}$ with respect to ECLIPJ2000 frame. In both figures, from left to right and top to bottom, semi-major axis a, eccentricity e, inclination i, RAAN Ω, argument of pericenter ω, and true anomaly θ are shown as a function of the time from the capture epoch t_0.

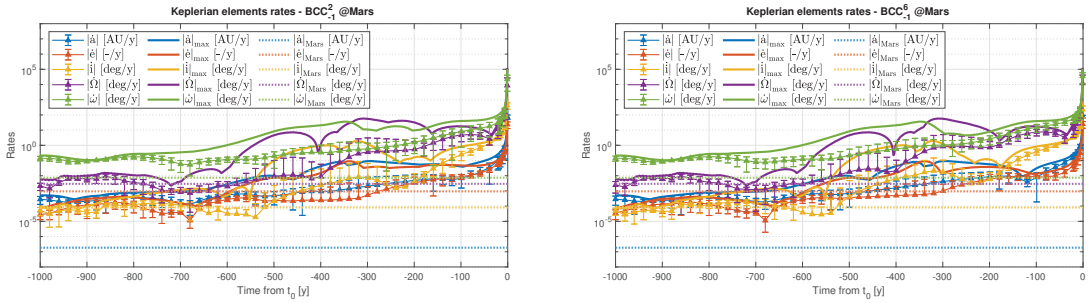

(a) Rates of heliocentric osculating elements of $\check{\mathcal{B}}^{2}_{-1}$.

(b) Rates of heliocentric osculating elements of $\check{\mathcal{B}}^{6}_{-1}$.

Figure 5. Rates of heliocentric osculating elements of BBCs from t_0 to t_0-1000 d with respect to ECLIPJ2000 frame. In both figures, triangles and error bars show the mean rates and their standard deviations, respectively. Solid lines represent the maximum rates, while dotted horizontal lines are the rates of Mars' orbit.

produce corridors whose time snapshots present poorly resolved, sparse, and large clusters which are hardly identifiable each other. Similar considerations can be done for the time snapshot in Figure 7 apart from the fact that only two clusters are identified. That because the other two branches are lost when imposing more revolutions and moving to the capture set $\mathcal{C}^{6}_{-1}$.

Step *iii*) opportunistic selection of a corridor subset

A subcorridor $\check{\mathcal{S}}^{6}_{-1}$ was built starting from the $\mathcal{C}^{6}_{-1}$ branch developing the interior corridor. Specifically, a circular domain within the capture set was opportunistically selected to fulfill the purpose. A circle of radius $\Delta r_p = 250$ km, and centered in $r_c = R_t + 3400$ km and $\omega_c = 250$ deg was constructed on the orbital plane of the capture set, as shown in Figure 8(a). The circle was placed at the top of the cluster because ICs are strongly regular in that region. Indeed, both regularity index and coefficient are small as shown by plots in Figure 2. In Figure 8(b), a magnification of the red circle in Figure 8(a) is reported.

Step *iv*) dimensions and shape of the subcorridor

The subcorridor dimensions and shape were studied backward propagating from t_0 to t_0-600 d the IC at the center and 20 ICs uniformly distributed along the border of the red circular domain in Figure 8. The resulting set of trajectories was used to build the corridor's envelope $\partial\check{\mathcal{S}}^{6}_{-1}$ in the physical space. The corridor is reported in Figures 9 and 10 from different points of view and in various reference frames.

Figure 9(a) shows the corridor, in light blue, from a top view of the xy-plane in the Sun-centered ECLIPJ2000 frame. The corridor was backward propagated from the capture epoch, visible in the bottom-left, for 600 days. That is almost a revolution period of Mars, whose orbit is plotted in black. The corridor remains closely attached to Mars's orbit and increases in size in backward time. The latter is a desirable feature, since it eases targeting the corridor for spacecraft with limited control authority like CubeSats. The corridor being a family of trajectories, its characteristics should be similar to what already discovered about single trajectories for Earth–Mars transfers with ballistic capture.[6]

The plot in Figure 9(b) offers a three-dimensional representation of the corridor in the Mars-centered ECLIPJ2000 frame. Far from Mars, the initial tiny circular region is stretched considerably. The envelope, initially shaped as a relatively small circle, increases remarkably in size and becomes almost a segment when backward propagated. That seems to reflect what observed in Figure 7, which shows thin and very long clusters of trajectories. Two-dimensional Mars-centered views of the corridor are provided in Figure 10. Specifically, Figure 10(a) collects the three views of the whole corridor, while Figure 10(b) offers magnifications of the corridor and post-capture* envelopes at a closer range from Mars.

*Trajectories of post-capture legs were obtained forward propagating the ICs on the border of the subcorridor domain from t_0 to

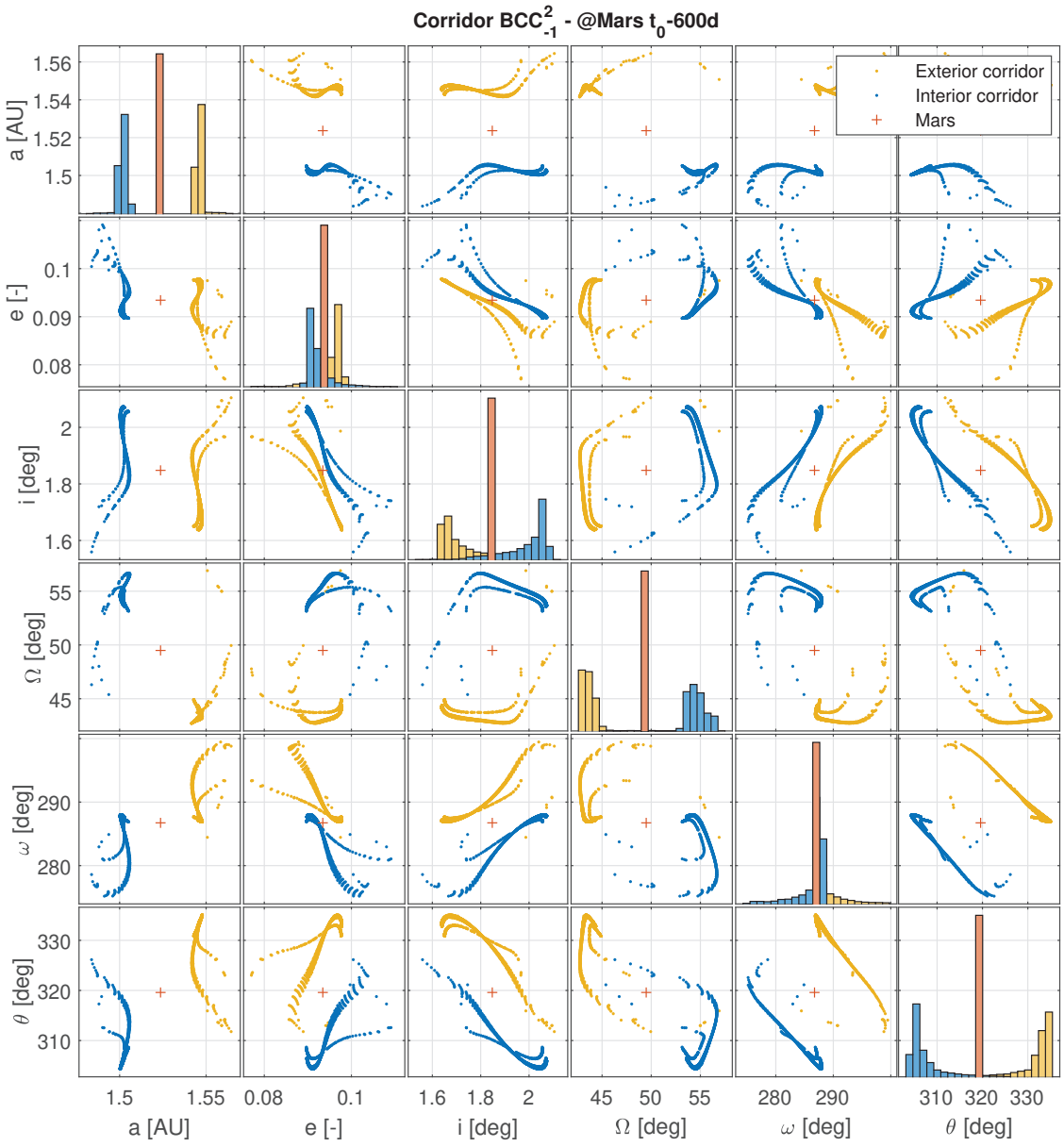

Figure 6. Time snapshot at $t_0-600\,\mathrm{d}$ of $\check{\mathcal{B}}^2_{-1}$. Scatterplot matrix of heliocentric osculating elements with respect to ECLIPJ2000 frame. The patterns of the two interior corridor branches, in blue, and the two exterior corridor branches, in yellow, are clearly visible. Red crosses represent Mars' Keplerian elements.

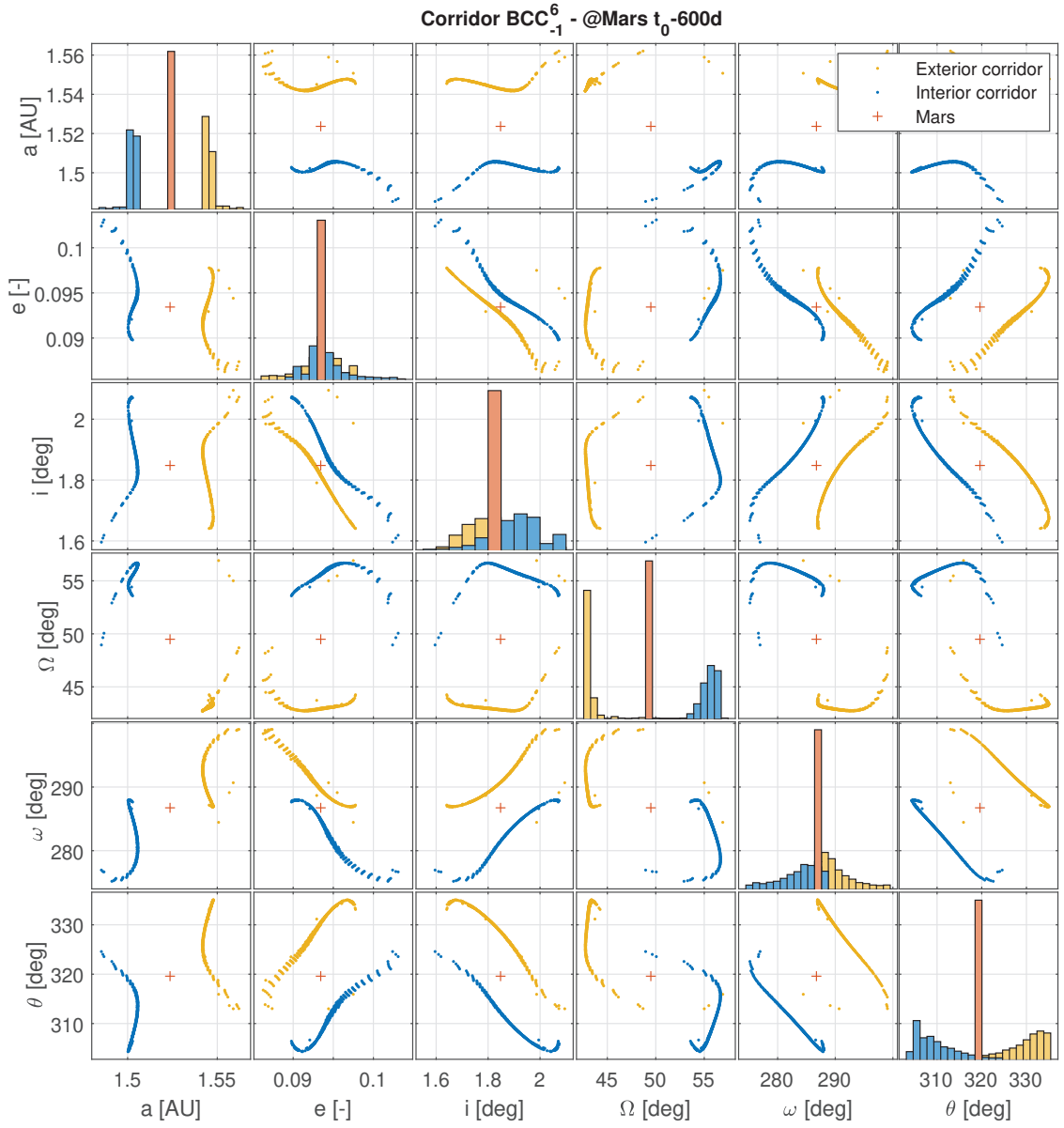

Figure 7. Time snapshot at $t_0-600\,\mathrm{d}$ of $\check{\mathcal{B}}^{6}_{-1}$. Scatterplot matrix of heliocentric osculating elements with respect to ECLIPJ2000 frame. The patterns of the only interior corridor branch, in blue, and the only exterior corridor branch, in yellow, are clearly identified. Red crosses represent Mars' Keplerian elements.

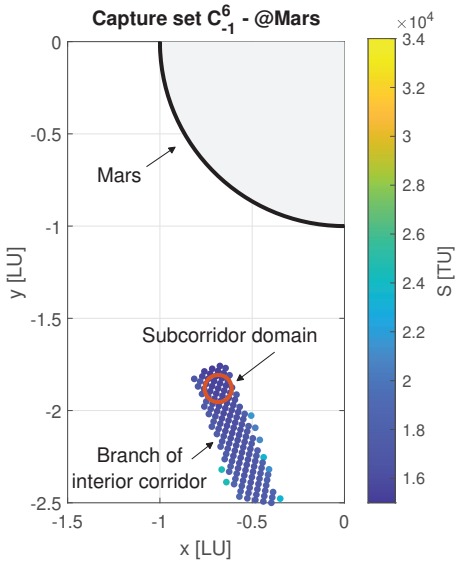

(a) Location of the circular domain opportunistically selected to build the subcorridor. The domain was located at the top of the cluster of ICs developing the interior corridor because that is a very regular region of the capture set. The diameter of the circular domain spans the cluster width almost completely.

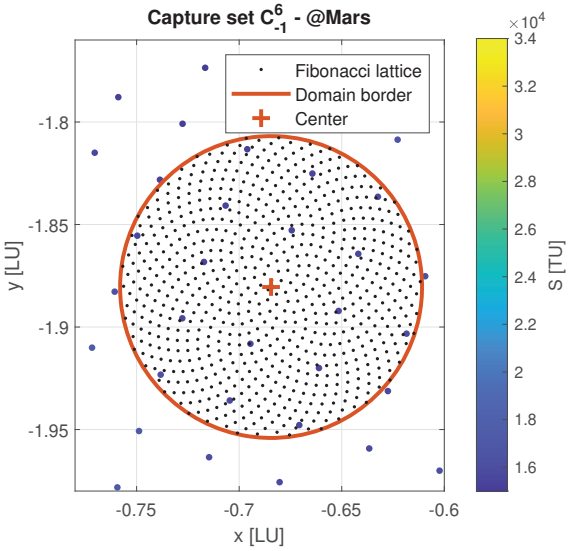

(b) Detail of circular subcorridor domain. The red solid curve and the red cross represents the domain's border and center, respectively. The black dots within the red surround represent an example 715 points Fibonacci lattice used to sample the subcorridor domain. Some points of capture set's grid can be seen in the background.

Figure 8. Details of capture set $\mathcal{C}^6_{-1}$ showing the regularity index of the ICs belonging to the set. ICs are represented in nondimensional quantities in the Mars-centered RTN@t_0 frame. Mars is partially shown in gray with black surround.

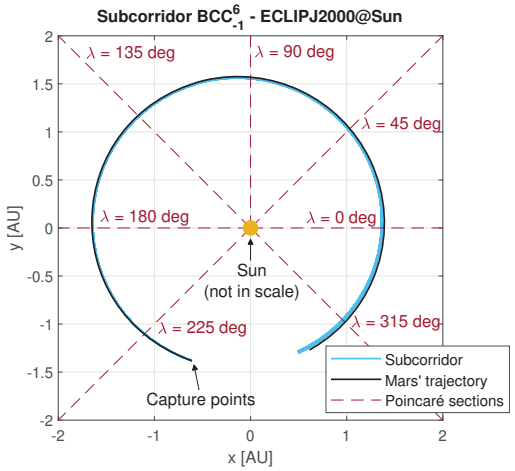

(a) Subcorridor envelope, in light blue, in the Sun-centered ECLIPJ2000 frame compared to Mars's orbit, in black. The dashed dark red half-lines, and the corresponding solar longitudes, identify the Poincaré sections shown in Figure 11.

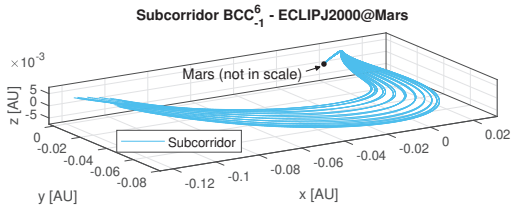

(b) Three-dimensional view of the subcorridor envelope in the Mars-centered ECLIPJ2000 frame.

Figure 9. Representations in the physical space of the subcorridor envelope $\partial\check{\mathcal{S}}^6_{-1}$ built from the red circular domain border shown in Figure 8. Envelope backward propagated from t_0 to t_0-600 d.

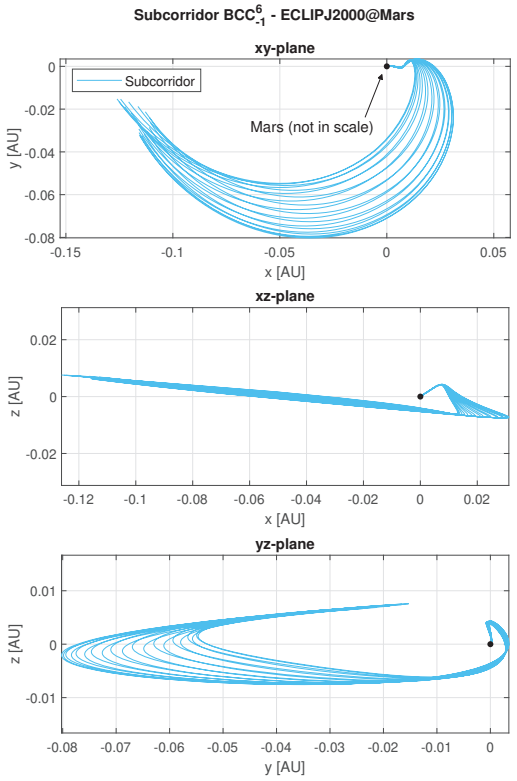

(a) Two-dimensional views of subcorridor envelope $\partial\check{\mathcal{S}}^{6}_{-1}$ far from Mars.

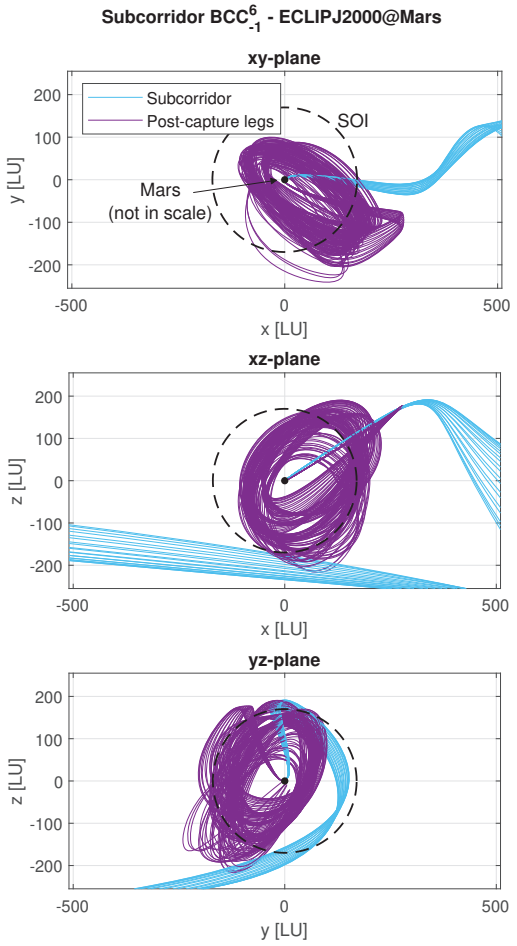

(b) Two-dimensional magnifications of subcorridor and post-capture envelopes at a closer range from Mars.

Figure 10. Representations in the physical space of the subcorridor envelope $\partial\check{\mathcal{S}}^{6}_{-1}$ built from the red circular domain border shown in Figure 8. Subcorridor backward propagated from t_0 to $t_0-600\,\mathrm{d}$. Trajectories plotted in the Mars-centered ECLIPJ2000 frame. In both figures, from top to bottom: xy-plane, xz-plane, and yz-plane.

Step *v*) subcorridor's Poincaré sections

Poincaré sections at prescribed solar longitudes of corridor's envelope (grid made of 100 ICs uniformly distributed along the border of the red circular domain in Figure 8) and center were computed to better understand how the envelope's shape changes over time and to estimate more precisely its characteristic dimensions. Seven half-planes in the physical space perpendicular to the *xy*-plane were selected at corresponding solar longitudes λ equal to 225 deg, 180 deg, 135 deg, 90 deg, 45 deg, 0 deg, and 315 deg. They are represented in Figure 9(a) as dashed red half-lines starting from the origin. The sequence is in accordance with the order in which the corridor crosses the Poincaré sections. The longitudes values were selected because they cover almost uniformly and completely the corridor from t_0 to t_0-600 d.

Results are shown in plots of Figure 11. They display Poincaré sections of positions and velocities of the envelope $\partial\check{\mathcal{S}}^6_{-1}$, marked by blue crosses, with respect to the corridor $\check{\mathcal{S}}^6_{-1}$ center, represented by the red diamond. Coordinates are computed in the ECLIPJ2000 frame. The sequence of Poincaré sections about positions allows to visualize how the envelope changes shape over time. In particular, its size at $\lambda = 315$ deg is more than one order of magnitude larger than its size at $\lambda = 225$ deg. At $\lambda = 90$ deg, the envelope twists around itself, while at $\lambda = 45$ deg it takes on a bizarre shape. Numerical experiments here excluded showed that around $\lambda = 90$ deg the corridor twists completely on itself. Differently, at around $\lambda = 45$ deg the top part of the envelope undergoes a deformation that resembles the movement of a waves. The twist lasts approximately from $\lambda = 105$ deg to $\lambda = 75$ deg, while the deformation persists roughly from $\lambda = 60$ deg to $\lambda = 30$ deg. Likely, such behaviors are the results of the peculiar distribution of Keplerian elements characterizing the trajectories belonging to the corridor and of how they geometrically interact in the physical space.

The characteristic dimensions of the envelope were retrieved from charts in Figure 11. Specifically, at $\lambda = 225$ deg, the two characteristic dimensions are approximately $d = 6.1 \times 10^{-5}$ AU (*i. e.,* the smaller dimension) and $D = 4.6 \times 10^{-4}$ AU (*i. e.,* the larger one). On the other hand, at $\lambda = 315$ deg, d and D are about 2.8×10^{-4} AU and 1.7×10^{-2} AU, respectively. In the latter case, d is relatively large ($\approx 4.2 \times 10^4$ km), albeit being two orders of magnitude smaller than D. That implies targeting a section perhaps large enough for limited control authority spacecraft, thereby proving that ballistic capture corridor targeting is a viable option for CubeSats.

The Sun-centered states of the points belonging to the envelope and shown in the Poincaré sections of Figure 11 can be retrieved summing the corresponding states of the center collected in Tables 3 and 4 (position and velocities, respectively). For the sake of completeness, time epochs and time intervals from t_0 of when the center crosses the sections are reported in Table 5. As an additional note, the center trajectory takes 224.76 days to escape from Mars in backward time. At the escape, the solar longitude is about 144 deg.

Step *vi*) subcorridor parametric representation and numerical approximation

The corridor was successfully represented through parametric surfaces. Figure 12 shows three sets of surfaces. They were obtained performing a Delaunay triangulation on a Fibonacci lattice of 105 points. The first set, in yellow, refers to a Poincaré section at $\lambda_1 = 90.05$ deg named *section 1*. The second one, colored in red and referred to as *section 2*, describes a Poincaré section at $\lambda_1 = 89.95$ deg. Finally, the blue set collects the parametric surfaces that were retrieved by linear interpolation of sections 1 and 2.

The center of the corridor was evaluated on all the seven Poincaré sections drawn in Figure 9(a). Two different corridor numerical approximations were tested, a coarse and a fine one. The former was built from Poincaré sections with step $\Delta\lambda = 0.1$ deg and approximated on Fibonacci lattice of 105 points* (see Figure 12 for an example approximation of this kind). The latter was derived from sections with step $\Delta\lambda = 0.01$ deg and Fibonacci lattice made of 715 points† (check Figure 8(b) to see how a 715 points Fibonacci lattice looks like).

$t_{f,\mathcal{W}_6}$. The latter being the time epoch at which the 6th revolution about the target body is achieved.

*To grant having 21 complete clockwise spirals made of 5 points each.

†To grant having 55 complete clockwise spirals made of 13 points each.

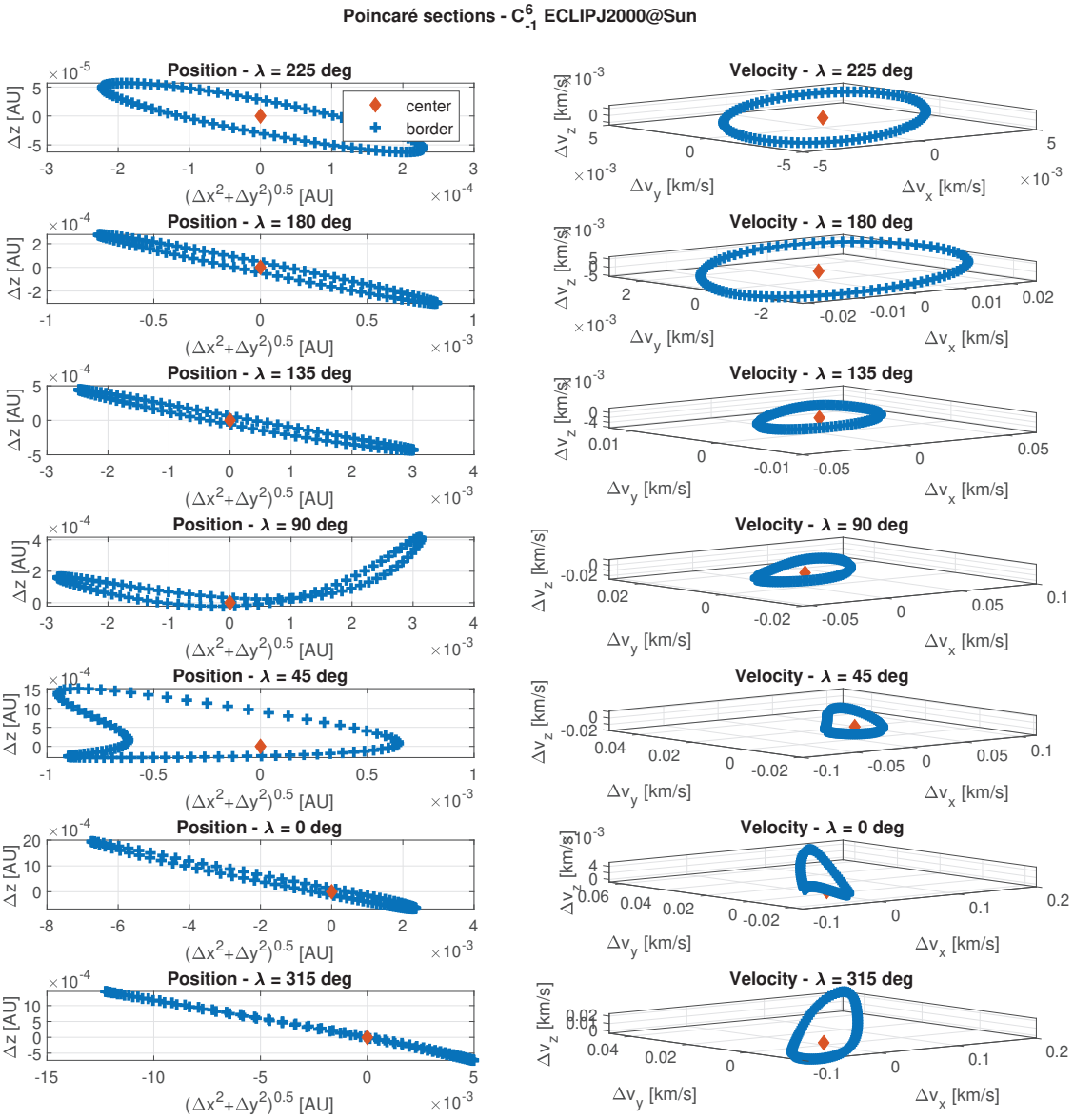

Figure 11. Poincaré sections of subcorridor $\check{\mathcal{S}}^{6}_{-1}$ in the ECLIPJ2000 frame for the various solar longitudes λ shown in Figure 9(a). Blue crosses represents points sampled on the subcorridor domain border. Center of circular domain identified by the red diamond. On the left, positions with respect to center. On the right, velocities with respect to the center. Time epochs, positions, and velocities of the center are collected in Tables 5, 3, and 4, respectively.

Table 3. Positions of center in Poincaré sections.

Solar longitude	Position		
λ (deg)	x (AU)	y (AU)	z (AU)
225	$-1.102\,808$	$-1.102\,808$	$7.844\,357 \times 10^{-3}$
180	$-1.641\,041$	$1.554\,104 \times 10^{-13}$	$4.293\,343 \times 10^{-2}$
135	$-1.162\,058$	$1.162\,058$	$5.006\,461 \times 10^{-2}$
90	$-6.957\,004 \times 10^{-15}$	$1.557\,277$	$2.662\,889 \times 10^{-2}$
45	$1.020\,845$	$1.020\,845$	$-8.854\,905 \times 10^{-3}$
0	$1.367\,875$	$7.111\,910 \times 10^{-13}$	$-3.521\,404 \times 10^{-2}$
315	$9.624\,945 \times 10^{-1}$	$-9.624\,945 \times 10^{-1}$	$-4.120\,283 \times 10^{-2}$

Table 4. Velocities of center in Poincaré sections.

Solar longitude	Velocity		
λ (deg)	v_x (km s^{-1})	v_y (km s^{-1})	v_z (km s^{-1})
225	$1.787\,586 \times 10^{1}$	$-1.510\,174 \times 10^{1}$	$-8.164\,564 \times 10^{-1}$
180	$8.595\,426 \times 10^{-1}$	$-2.222\,691 \times 10^{1}$	$-4.055\,608 \times 10^{-1}$
135	$-1.623\,405 \times 10^{1}$	$-1.507\,938 \times 10^{1}$	$1.683\,084 \times 10^{-1}$
90	$-2.333\,669 \times 10^{1}$	$2.152\,594$	$6.396\,673 \times 10^{-1}$
45	$-1.617\,810 \times 10^{1}$	$1.940\,766 \times 10^{1}$	$7.479\,764 \times 10^{-1}$
0	$1.080\,975$	$2.655\,486 \times 10^{1}$	$4.253\,387 \times 10^{-1}$
315	$1.832\,666 \times 10^{1}$	$1.940\,964 \times 10^{1}$	$-1.405\,752 \times 10^{-1}$

Table 5. Time epochs and time intervals from t_0 at which center crosses Poincaré sections.

Solar longitude	Time epoch	Time interval from t_0
λ (deg)	t_c (UTC)	$t_c - t_0$ (d)
225	28 OCT 2023 11:14:06.557	-41.563
180	24 JUL 2023 08:52:44.062	-137.66
135	13 APR 2023 16:33:00.264	-239.34
90	07 JAN 2023 05:22:50.146	-335.81
45	15 OCT 2022 00:19:38.723	-420.02
0	02 AUG 2022 12:51:56.425	-493.50
315	25 MAY 2022 11:05:11.527	-562.57

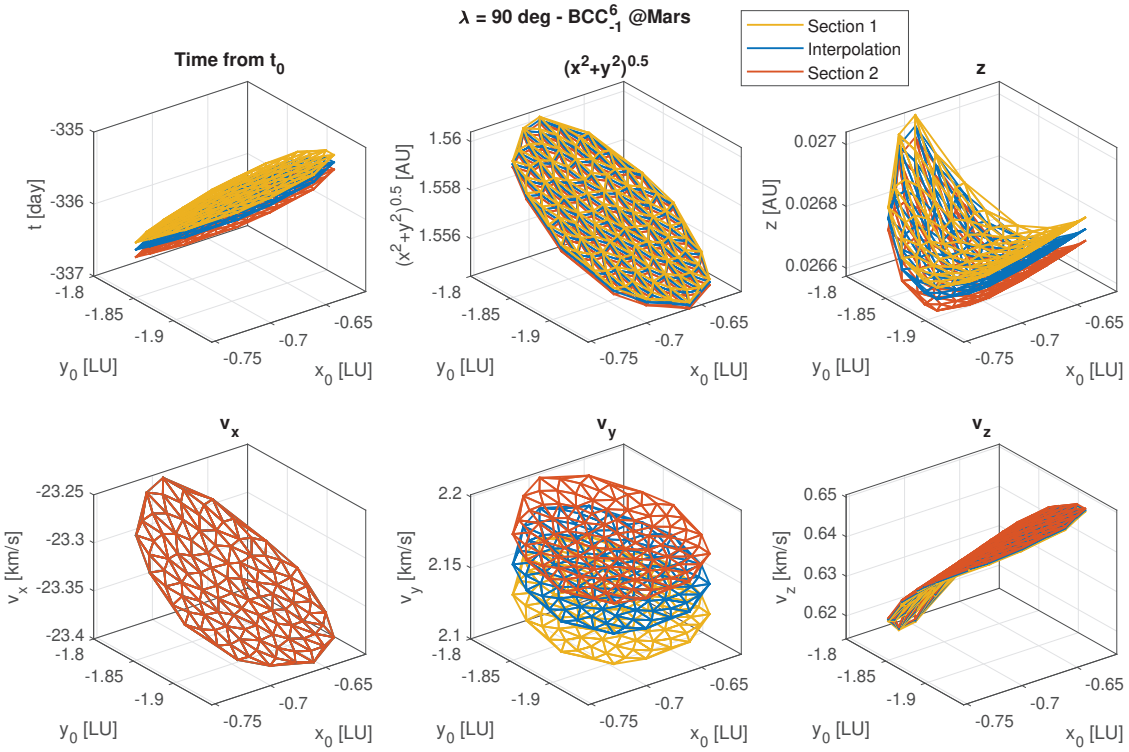

Figure 12. Parametric surfaces of subcorridor's time epoch and Cartesian states at three different Poincaré sections. Cartesian states in the Sun-centered ECLIPJ2000 frame. The parameters are the two independent Cartesian coordinates x_0 and y_0 of the capture set orbital plane. The yellow and red surfaces located at solar longitudes $\lambda_1 = 90.05\,\text{deg}$ and $\lambda_1 = 89.95\,\text{deg}$, respectively, were used to linearly interpolate the blue one at $\lambda_1 = 90\,\text{deg}$.

The test point evaluations were compared against the high-fidelity solution propagated with GRATIS (collected in Table 3 and Table 4). The errors at insertion were computed for any tested solar longitudes. Results are shown in the left plot of Figure 13(a). The right plot provides the errors at capture. Figure 13(b) reports the same errors when using the fine approximation.

As expected, the fine approximation performs better, overall granting smaller errors than the coarse one both at insertion and capture. Errors are larger when interpolating far from capture, likely because of the stretching phenomenon observed in the Poincaré sections shown in Figure 11. However, they seem to stabilize after the corridor crosses the Poincaré section at $\lambda = 90\,\text{deg}$. Regarding errors on time epoch and velocity at insertion, they seem to exhibit local maxima in correspondence of the corridor twisting, when $\lambda \approx 90\,\text{deg}$.

CONCLUSION

This work presents the first step in the development of an on-board autonomous ballistic capture algorithm suitable for spacecraft with limited control authority and resources like CubeSats. The characterization of ballistic capture corridors, in particular the mapping of capture conditions to interplanetary states, is the first effort to engineer BC in a completely autonomous fashion. Future work will be focused on providing a formal mathematical definitions of BCCs and associated entities. Additionally, a proper Monte Carlo analysis will be carried out to assess robustness to capture of corridor numerical approximations for increasing levels of refinement. Different interpolation schemes will be tested to find the best trade-off between computational effort and accuracy. Indeed, numerical experiments here omitted showed how too coarse approximations

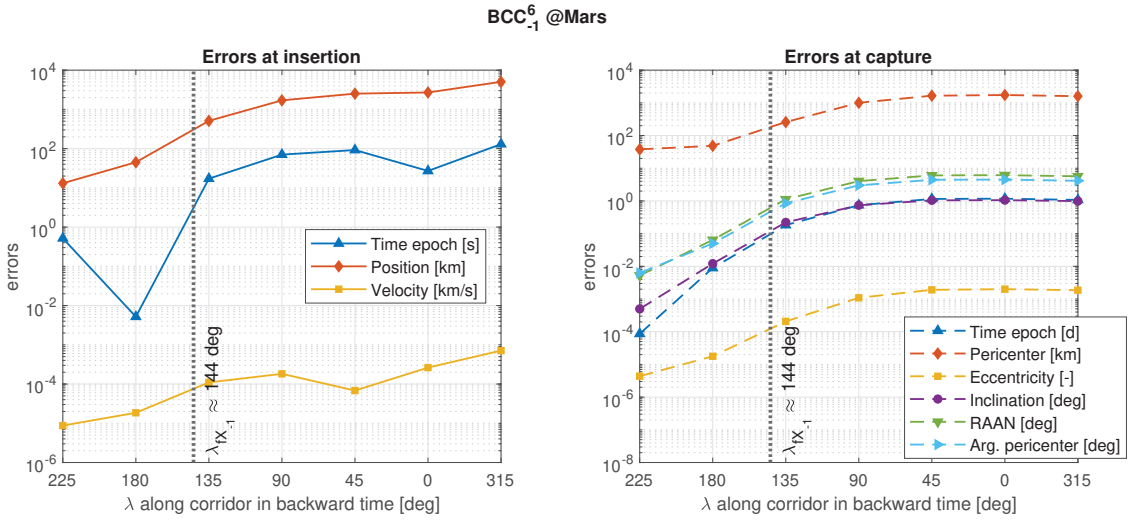

(a) Errors when coarsely approximating the subcorridor with step $\Delta\lambda = 0.1$ deg and a 105 points Fibonacci lattice.

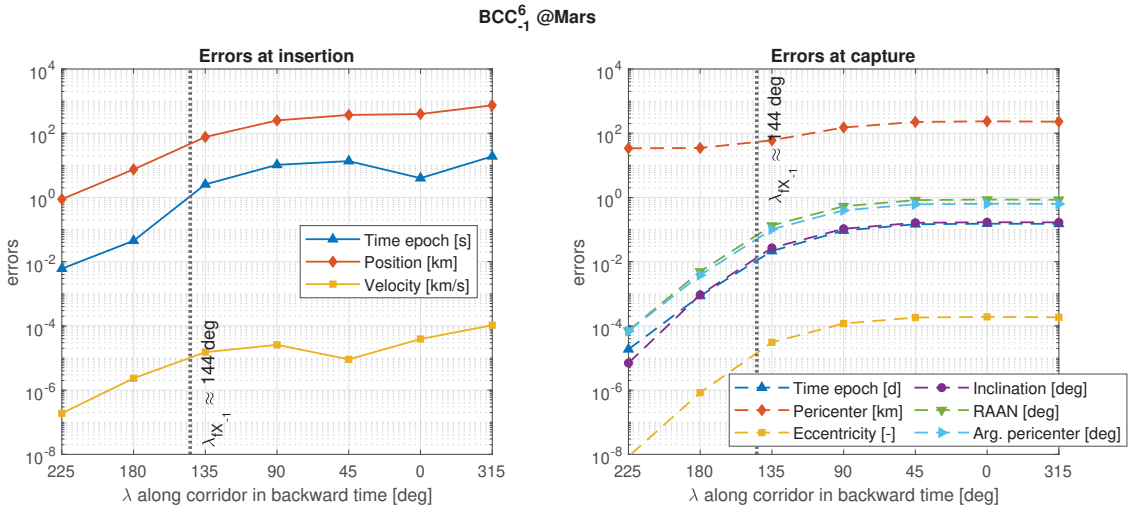

(b) Errors when finely approximating the subcorridor with step $\Delta\lambda = 0.01$ deg and a 715 points Fibonacci lattice.

Figure 13. Errors at insertion on the subcorridor $\check{\mathcal{S}}^6_{-1}$, on the left, and at capture point, on the right. The dotted black vertical lines mark the approximate solar longitude $\lambda_{f\mathcal{X}_{-1}}$ at which a spacecraft escapes from Mars when flying on the subcorridor's center trajectory in backward time. The x-axes are not monotone increasing because they represent the solar longitude λ wrapped to $360\,\mathrm{deg}$ along the subcorridor in backward time.

failed in representing correctly corridors. In particular, approximations seem really sensitive to the step $\Delta\lambda$ used for reconstructing intermediate Poincaré sections. Alternative interpolation techniques like cubic spline or cubic convolution are expected to perform better than the simple, fast linear interpolation. That at the drawback of large computation efforts required both in terms of memory and time. Specifically, cubic convolution interpolation was already proven successful when trying to approximate invariant manifolds in the restricted circular three body problem.[34] The discussed corridor numerical approximation will be refined and employed to build a database of BCCs. Database that the guidance algorithm under development in the EXTREMA project will exploit to achieve autonomous BC at Mars. Finally, attainability of BCCs pathways as viable options for autonomous CubeSats to achieve temporary capture at major planets according to their knowledge and dispersion errors will be analyzed.

ACKNOWLEDGMENT

This work has received funding from the European Research Council (ERC) under the European Union's Horizon 2020 research and innovation programme (grant agreement No. 864697).

REFERENCES

[1] S. Bandyopadhyay, R. Foust, G. P. Subramanian, S.-J. Chung, and F. Y. Hadaegh, "Review of formation flying and constellation missions using nanosatellites," *Journal of Spacecraft and Rockets*, Vol. 53, No. 3, 2016, pp. 567–578. 10.2514/1.a33291.

[2] H. Kalita, E. Asphaug, S. Schwartz, and J. Thangavelautham, "Network of Nano-Landers for In-Situ characterization of asteroid impact studies," 2017. arXiv:1709.02885.

[3] A. M. Hein, M. Saidani, and H. Tollu, "Exploring potential environmental benefits of asteroid mining," *69th International Astronautical Congress 2018*, 2018. arXiv:1810.04749.

[4] E. A. Belbruno and J. K. Miller, "Sun-perturbed Earth-to-moon transfers with ballistic capture," *Journal of Guidance, Control, and Dynamics*, Vol. 16, jul 1993, pp. 770–775. 10.2514/3.21079.

[5] E. Belbruno and J. Carrico, "Calculation of weak stability boundary ballistic lunar transfer trajectories," *Astrodynamics Specialist Conference*, 2000, p. 4142. 10.2514/6.2000-4142.

[6] F. Topputo and E. Belbruno, "Earth–Mars transfers with ballistic capture," *Celestial Mechanics and Dynamical Astronomy*, Vol. 121, No. 4, 2015, pp. 329–346. 10.1007/s10569-015-9605-8.

[7] C. Circi and P. Teofilatto, "On the dynamics of weak stability boundary lunar transfers," *Celestial Mechanics and Dynamical Astronomy*, Vol. 79, No. 1, 2001, pp. 41–72. 10.1023/A:1011153610564.

[8] V. V. Ivashkin, "On trajectories of Earth-Moon flight of a particle with its temporary capture by the Moon," *Doklady Physics*, Vol. 47, Springer, 2002, pp. 825–827. 10.1134/1.1526433.

[9] E. A. Belbruno and J. Miller, "A ballistic lunar capture trajectory for the Japanese spacecraft hiten," tech. rep., 1990. IOM 312/904-1731-EAB.

[10] G. D. Racca, A. Marini, L. Stagnaro, J. Van Dooren, L. Di Napoli, B. H. Foing, R. Lumb, J. Volp, J. Brinkmann, R. Grünagel, *et al.*, "SMART-1 mission description and development status," *Planetary and space science*, Vol. 50, No. 14-15, 2002, pp. 1323–1337. 10.1016/S0032-0633(02)00123-X.

[11] M. J. Chung, S. J. Hatch, J. A. Kangas, S. M. Long, R. B. Roncoli, and T. H. Sweetser, "Trans-lunar cruise trajectory design of GRAIL (Gravity Recovery and Interior Laboratory) mission," *AIAA/AAS Astrodynamics Specialist Conference*, 2010, p. 8384. 10.2514/6.2010-8384.

[12] R. Jehn, S. Campagnola, D. Garcia, and S. Kemble, "Low-thrust approach and gravitational capture at Mercury," *18th International Symposium on Space Flight Dynamics*, Vol. 548, 2004, p. 487.

[13] J. Elliott and L. Alkalai, "Lunette: A network of lunar landers for in-situ geophysical science," *Acta Astronautica*, Vol. 68, No. 7-8, 2011, pp. 1201–1207. 10.1016/j.actaastro.2010.10.024.

[14] M. Vetrisano, W. V. d. Weg, and M. Vasile, "Navigating to the Moon along low-energy transfers," *Celestial Mechanics and Dynamical Astronomy*, Vol. 114, No. 1, 2012, pp. 25–53. 10.1007/s10569-012-9436-9.

[15] E. Belbruno, *Capture Dynamics and Chaotic Motions in Celestial Mechanics*. Princeton University Press, dec 2004. 10.1515/9780691186436.

[16] F. Topputo and E. Belbruno, "Computation of weak stability boundaries: Sun–Jupiter system," *Celestial Mechanics and Dynamical Astronomy*, Vol. 105, No. 1-3, 2009, p. 3. 10.1007/s10569-009-9222-5.

[17] Z.-F. Luo and F. Topputo, "Analysis of ballistic capture in Sun–planet models," *Advances in Space Research*, Vol. 56, No. 6, 2015, pp. 1030–1041. 10.1016/j.asr.2015.05.042.

[18] Z.-F. Luo, F. Topputo, F. Bernelli Zazzera, and G. J. Tang, "Constructing ballistic capture orbits in the real Solar System model," *Celestial Mechanics and Dynamical Astronomy*, Vol. 120, No. 4, 2014, pp. 433–450. 10.1007/s10569-014-9580-5.

[19] B. A. Archinal, M. F. A'Hearn, E. Bowell, A. Conrad, G. J. Consolmagno, R. Courtin, T. Fukushima, D. Hestroffer, J. L. Hilton, G. A. Krasinsky, *et al.*, "Report of the IAU working group on cartographic coordinates and rotational elements: 2009," *Celestial Mechanics and Dynamical Astronomy*, Vol. 109, No. 2, 2011, pp. 101–135. 10.1007/s10569-010-9320-4.

[20] C. H. Acton Jr, "Ancillary data services of NASA's navigation and ancillary information facility," *Planetary and Space Science*, Vol. 44, No. 1, 1996, pp. 65–70. 10.1016/0032-0633(95)00107-7.

[21] C. Acton, N. Bachman, B. Semenov, and E. Wright, "A look towards the future in the handling of space science mission geometry," *Planetary and Space Science*, Vol. 150, 2018, pp. 9–12. 10.1016/j.pss.2017.02.013.

[22] G. Gómez, A. Jorba, J. Masdemont, and C. Simó, "Study of the transfer from the Earth to a halo orbit around the equilibrium point L1," *Celestial Mechanics and Dynamical Astronomy*, Vol. 56, No. 4, 1993, pp. 541–562. 10.1007/BF00696185.

[23] R. S. Park, W. M. Folkner, J. G. Williams, and D. H. Boggs, "The JPL Planetary and Lunar Ephemerides DE440 and DE441," *The Astronomical Journal*, Vol. 161, No. 3, 2021, p. 105. 10.3847/1538-3881/abd414.

[24] F. Topputo, Y. Wang, C. Giordano, V. Franzese, H. Goldberg, F. Perez-Lissi, and R. Walker, "Envelop of reachable asteroids by M-ARGO CubeSat," *Advances in Space Research*, Vol. 67, No. 12, 2021, pp. 4193–4221. 10.1016/j.asr.2021.02.031.

[25] G. Aguiar, F. Topputo, *et al.*, "A Technique for Designing Earth-Mars Low-Thrust Transfers Culminating in Ballistic Capture," *7th International Conference on Astrodynamics Tools and Techniques (ICATT)*, 2018, pp. 1–8.

[26] R. G. Gottlieb, "Fast gravity, gravity partials, normalized gravity, gravity gradient torque and magnetic field: Derivation, code and data," tech. rep., 1993. 188243, prepared for Lyndon B. Johnson Space Center under contract NAS9-17885.

[27] F. Topputo, D. A. Dei Tos, K. V. Mani, S. Ceccherini, C. Giordano, V. Franzese, and Y. Wang, "Trajectory design in high-fidelity models," *7th International Conference on Astrodynamics Tools and Techniques (ICATT)*, 2018, pp. 1–9.

[28] L. F. Shampine and M. W. Reichelt, "The matlab ode suite," *SIAM journal on scientific computing*, Vol. 18, No. 1, 1997, pp. 1–22, 10.1137/s1064827594276424.

[29] O. Montenbruck and E. Gill, *Satellite Orbits Models, Methods and Applications*. Springer, 2000. 10.1007/978-3-642-58351-3.

[30] P. J. Prince and J. R. Dormand, "High order embedded Runge-Kutta formulae," *Journal of computational and applied mathematics*, Vol. 7, No. 1, 1981, pp. 67–75. 10.1016/0771-050x(81)90010-3.

[31] P. A. Sousa Silva and M. O. Terra, "Diversity and validity of stable-unstable transitions in the algorithmic weak stability boundary," *Celestial Mechanics and Dynamical Astronomy*, Vol. 113, No. 4, 2012, pp. 453–478. 10.1007/s10569-012-9418-y.

[32] Z. F. Luo and F. Topputo, "Capability of satellite-aided ballistic capture," *Communications in Nonlinear Science and Numerical Simulation*, Vol. 48, 2017, pp. 211–223. 10.1016/j.cnsns.2016.12.021.

[33] D. A. Dei Tos, R. P. Russell, and F. Topputo, "Survey of Mars ballistic capture trajectories using periodic orbits as generating mechanisms," *Journal of Guidance, Control, and Dynamics*, Vol. 41, No. 6, 2018, pp. 1227–1242. 10.2514/1.g003158.

[34] F. Topputo, "Fast numerical approximation of invariant manifolds in the circular restricted three-body problem," *Communications in Nonlinear Science and Numerical Simulation*, Vol. 32, 2016, pp. 89–98. 10.1016/j.cnsns.2015.08.004.

[35] R. Swinbank and R. J. Purser, "Fibonacci grids: A novel approach to global modelling," *Quarterly Journal of the Royal Meteorological Society: A journal of the atmospheric sciences, applied meteorology and physical oceanography*, Vol. 132, No. 619, 2006, p. 1769–1793, 10.1256/qj.05.227.

[36] N. Hyeraci and F. Topputo, "Method to design ballistic capture in the elliptic restricted three-body problem," *Journal of guidance, control, and dynamics*, Vol. 33, No. 6, 2010, pp. 1814–1823. 10.2514/1.49263.